Appl Phys A (2009) 94: 139–154
DOI 10.1007/s00339-008-4685-x

Applied Physics A
Materials Science & Processing

Amorphous stainless steel coatings prepared by reactive magnetron-sputtering from austenitic stainless steel targets

Salvatore Cusenza · Peter Schaaf

Received: 17 March 2008 / Accepted: 22 May 2008 / Published online: 13 June 2008

Abstract Stainless steel films were reactively magnetron sputtered in argon/methane gas flow onto oxidized silicon wafers using austenitic stainless-steel targets. The deposited films of about 200 nm thickness were characterized by conversion electron Mössbauer spectroscopy, magneto–optical Kerr-effect, X-ray diffraction, scanning electron microscopy, Rutherford backscattering spectrometry, atomic force microscopy, corrosion resistance tests, and Raman spectroscopy. These complementary methods were used for a detailed examination of the carburization effects in the sputtered stainless-steel films. The formation of an amorphous and soft ferromagnetic phase in a wide range of the processing parameters was found. Further, the influence of the substrate temperature and of post vacuum-annealing were examined to achieve a comprehensive understanding of the carburization process and phase formation.

PACS 81.15.Cd · 81.65.Lp · 82.80.Ej · 61.43.Dq · 68.55.Jk

1 Introduction

Carburized steels are of great technical interest but also of high complexity, considering the existence of a stable Fe–graphite and the metastable Fe–cementite system [1–3] in combination with a large number of alloying elements. Different carburization techniques are in use, where a carbon-containing ambient is transferred into a solid solution of carbon in the metal [4] or carbide formation. Usually this leads to a well-established equilibrium between ambient and dissolved carbon. There are carburization processes in which hardening steels are treated at high temperatures (>1000 K) using endogas or natural atmospheres (e.g., methane) [4]. After carburizing, various carbides were observed in steels such as M_3C, M_7C_3, $M_{23}C_6$, and M_6C [5–11]. Even though there are many studies dealing with such carburizing processes, their ruling phenomena are still quite unclear, especially for stainless steels.

Recent studies report on the amorphization of steels [12–14]; however, these steels are not really classical steels. Unusual alloying elements such as Y, Zr, and B were used in these experiments. From an industrial point of view, amorphous steels would be of great interest with respect to friction, wear, corrosion, and further properties.

Here, the reactive magnetron sputtering technique is used, where carbon incorporation is implemented in the magnetron via a reactive methane/argon sputtering plasma. Conventional austenitic stainless steels (AISI 310 and AISI 316) were used for this study. The presentation here focuses on the results for AISI 316.

2 Experimental

2.1 Reactive sputter deposition

The films were sputter-deposited with an rf magnetron onto amorphous SiO_2 substrates (oxidized Si(100) wafer of 0.5 mm thickness, pre-cleaned with acetone and oxidized

P. Schaaf's former affiliation: II. Physikalisches Institut, Universität Göttingen, Friedrich-Hund-Platz 1, 37077 Göttingen, Germany.

S. Cusenza
II. Physikalisches Institut, Universität Göttingen,
Friedrich-Hund-Platz 1, 37077 Göttingen, Germany
e-mail: scusenz@uni-goettingen.de

P. Schaaf (✉)
Institut für Werkstofftechnik, FG Werkstoffe der Elektrotechnik,
TU Ilmenau, Postfach 10 05 65, 98684, Ilmenau, Germany
e-mail: peter.schaaf@tu-ilmenau.de

Table 1 Gas flow j, deposition time t, real film thickness d (as measured by Rutherford Backscattering Spectrometry (RBS) after deposition) and derived growth rate $g = \frac{d}{t}$ for the deposited carburized films. All samples were deposited at 298 K with a magnetron power of 100 W and a target-substrate distance of 10 cm

Sample	j_{CH_4} [sccm]	j_{Ar} [sccm]	t [min]	d [nm]	g [nm/min]
M0	0.00	12.00	17:00	205(10)	12.06(92)
M1	0.01	11.99	19.49	242(10)	12.21(84)
M5	0.05	11.95	20:24	220(10)	10.78(74)
M10	0.10	11.90	19:43	238(10)	12.07(83)
M50	0.50	11.50	27:43	208(10)	7.50(46)
M75	0.75	11.25	31:12	216(10)	6.92(39)
M100	1.00	11.00	33:29	222(10)	6.63(36)
M125	1.25	10.75	37:40	267(10)	7.09(33)

in air, no further treatment) utilizing commercial AISI 316 (X5CrNiMo17-12-2, 1.4401) and AISI 310 (X8CrNi25-21, 1.4845) targets. The target–substrate distance was set to 10 cm. The processing parameters were always 100 W magnetron power at a constant total gas flow of 12 sccm (sccm = standard cubic centimeter, i.e., flow volume of gas at normal conditions, 273.15 K and 1013 hPa) during deposition. Several sample series were deposited at different CH_4 flows (0.00–1.25 sccm). The sputter rate was always in the range of 0.1–0.2 nm/s, and was depending on the processing parameters. The magnetron chamber was evacuated to a base pressure of 10^{-4} Pa before deposition. The target was always pre-sputtered for half an hour with the desired parameters before starting the deposition onto the substrate. The target was water cooled and the substrate temperature was controlled between room temperature (water cooling) and 673 K (electrical heating). The thickness of the deposited films was controlled by a quartz microbalance (with a film density set to 7.89 kg/m^3, which is the density of AISI 316). We tried to deposit samples with similar thicknesses as given by the quartz microbalance. As a result, deposition time and real film thickness varied. The deposition parameters and the resulting thicknesses and growth rates are summarized in Table 1.

From these data it is derived that the growth rate is decreasing with increasing CH_4 flow what is visualized in Fig. 1. The growth rate drops more or less exponentially from about 12 nm/min for the inert sputtering to half of this value for higher methane flows. This might be due to the varying sputtering rates induced by the carbon uptake into the surface of the sputtering target.

2.2 Analysis methods

Phase analysis for the deposited films by conversion electron Mössbauer spectroscopy (CEMS) was performed at room

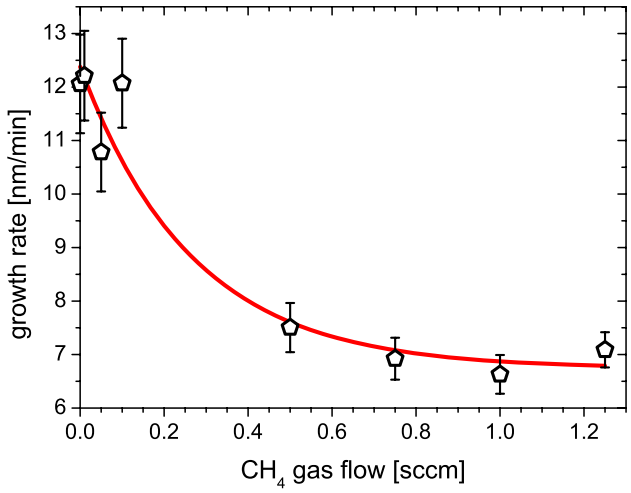

Fig. 1 Growth rate g as a function of the CH_4 gas flow j_{CH_4} for the room temperature deposition

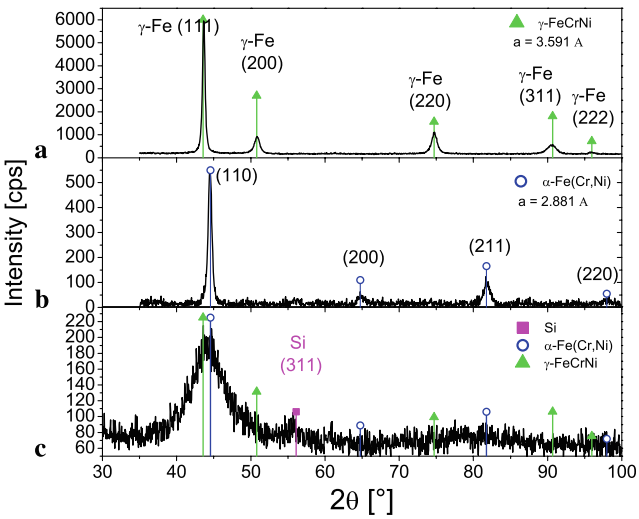

Fig. 2 XRD spectra: (**a**) $\theta - 2\theta$ pattern of the AISI 316 sputter target; (**b**) GIXRD (2° incidence angle) pattern of the film sputtered from the AISI 316 target at room temperature with a magnetron power of 100 W and with a pure Ar gas flow of 12 sccm; (**c**) with a gas flow of 11.99 sccm Ar and 0.01 sccm methane. The reflexes of the γ and α phases are indexed. The peak in (**c**) at about 56° corresponds to the Si substrate

temperature, employing a ^{57}Co/Rh source in constant acceleration mode [15–17]. The electrons were detected in a He/CH_4 flow proportional counter [18–20]. The spectra were fitted by a hyperfine field distribution calculated with the Normos code [21] or by superimposing Lorentzian lines with the WinISO fitting tool [22]. The velocity calibration was carried out using α-Fe foil and the isomer shifts are given relative to the center of this calibration.

Magneto–optical Kerr effect (MOKE) was used to investigate the ferromagnetic behavior of the samples. The measurements were conducted in longitudinal geometry

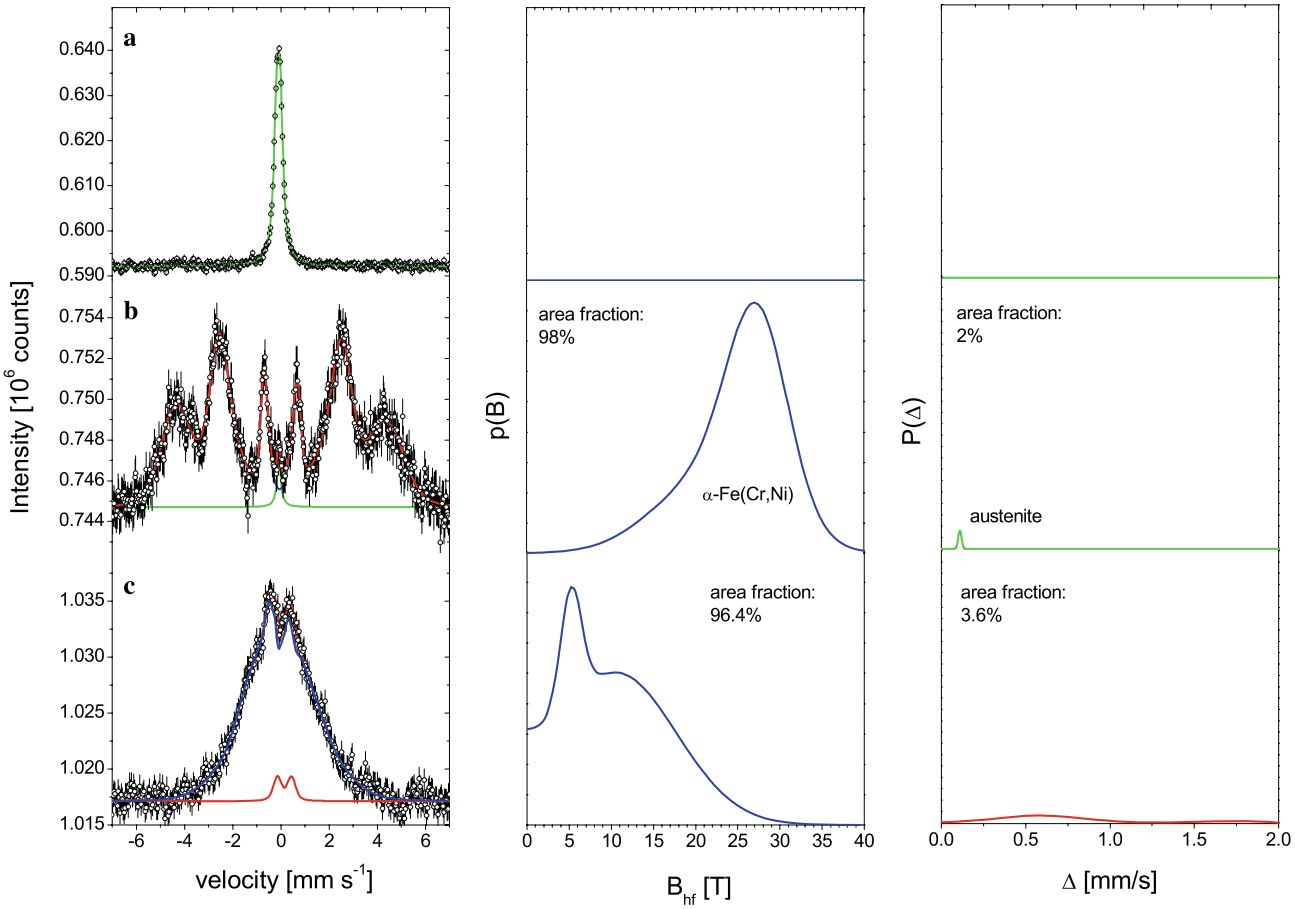

Fig. 3 CEM spectra of: (**a**) the original AISI 316 sputter target; (**b**) the film sputtered from this target at room temperature with a magnetron power of 100 W and with a pure Ar gas flow of 12 sccm; (**c**) with a gas flow of 11.99 sccm Ar and 0.01 sccm methane. The corresponding distributions of the hyperfine field $p(B)$ are given in the middle, the distributions of the quadrupole splitting $p(\Delta)$ on the right

and at room temperature, using a polarization-compensator–sample–analyzer (PCSA) ellipsometer and a maximum external magnetic field of 0.15 T [23, 24]. The samples were mounted onto a rotationally motorized holder, so that magnetic anisotropy could also be analyzed by rotating the sample with respect to the direction of the magnetic field [25].

Crystallographic analyses were performed by grazing incidence X-ray diffraction (GIXRD) using a Bruker AXS D8 diffractometer equipped with a Cu-Kα source ($\lambda = 1.54$ Å) and a grazing incidence attachment. The incident angle was fixed at 2° for thin film measurements. Scanning electron microscopy (SEM) was carried out employing a Philips SEM 515 with an acceleration voltage of 0.2 to 30 kV. Its resolution is limited to 5 nm and it is equipped with an Everhart–Thornley secondary electron detector, a Robinson backscattered electron detector, and a digital EDX prism X-ray detector for energy-dispersive X-ray analyses (EDX).

Rutherford backscattering spectrometry (RBS) was performed at the 530 kV IONAS [26] accelerator facility in Göttingen, using a 900 keV He^{2+} beam and a backscattering angle of 165°. Atomic force microscopy (AFM) was performed on a Nanoscope III MultiMode AFM (Digital Instruments) whose maximum scan range is 80 µm × 80 µm. All samples were measured in tapping-mode.

Corrosion resistance tests used a combination of two galvanic cells. The sputtered films were used as working electrodes, a platinum and calomel electrode as counter- and as reference-electrode, respectively. 1-molar Na_2SO_4 was used as electrolyte and the voltage was varied from −2 to +2 V by means of a potentiostat.

Raman spectroscopy was carried out on a self assembled device. An argon laser with a wavelength of 514.5 nm was used, together with a Dilor XY triple monochromator. The optics track was assigned to the so-called macro-Raman optics in which the laser beam is aligned in grazing incident mode. The emitted Raman radiation was mapped by a CCD camera.

Nanoindentation measurements were performed on a Fischerscope HV100 with a Vickers diamond. The maximum indention force was set to 5 mN. Five positions were measured for each sample and the mean values are reported [27].

3 Results

3.1 Deposition at room temperature

3.1.1 Target material, inert and reactive sputtered films

The original AISI 316 targets have a face-centered cubic (fcc, γ) structure, in contrast to inert magnetron-sputtered thin AISI 316 films, which exhibit body-centered cubic (bcc, α) structure when deposited below 678 K [28]. This is readily seen in Fig. 2.

The fcc structure of the original target and the bcc structure of the resulting inert sputtered are extracted from Fig. 2(a) and (b). The lattice constants obtained are $a = 0.3592(1)$ nm for the fcc and $a = 0.2881(1)$ nm for the bcc films. As shown in Fig. 2(c), no clear narrow reflexes were observed in the carburized magnetron sputtered stainless-steel film for sample M1. Only a small (311) reflex from the Si(100) wafer occurs in GIXRD. So the reactive sputtered and thus carburized film exhibits an amorphous structure in the X-ray diffraction pattern.

This behavior is resembled in the Mössbauer spectra of the samples as shown in Fig. 3.

The Mössbauer spectrum of the original AISI 316 target in Fig. 3(a) shows the typical non-magnetic central line of austenite with an isomer shift of $\delta = -0.10(1)$ mm/s [29].

The inert sputtered AISI 316 film in Fig. 3(b) shows a broad magnetically split sextet, which is consistent with the observed bcc structure in XRD and the given Chromium and Nickel content in the film [8, 30]. From the fitting, a mean hyperfine field of $\langle B \rangle = 25.2$ T with a width of $\sigma = 5.8$ T is obtained from the $p(B)$ distribution. In addition, a small contribution of austenite with an area fraction of $f_A = 2(1)\%$ is resolved.

The CEM spectrum of the reactive sputtered film in Fig. 3(c) shows also a broad magnetically split sextet and a small contribution of a broad paramagnetic doublet. The bimodal distribution $p(B)$ might be due to two different coordination parts in the film, one with low C content and one with high C content.

3.1.2 Influence of methane gas flow

The methane gas flow was systematically increased from 0.01 sccm to 1.25 sccm. For all these deposited films, the reactive magnetron deposited and carburized samples show the typical broad XRD appearance of amorphous materials, as seen in Fig. 4. These diffractograms show a clear amorphous signature.

Figure 5 shows the position and the width of the first broad peak for the spectra shown in Fig. 4. There is a clear tendency for peak position and peak width, where the peak position is decreasing and the peak width is increasing with increasing CH_4 flow.

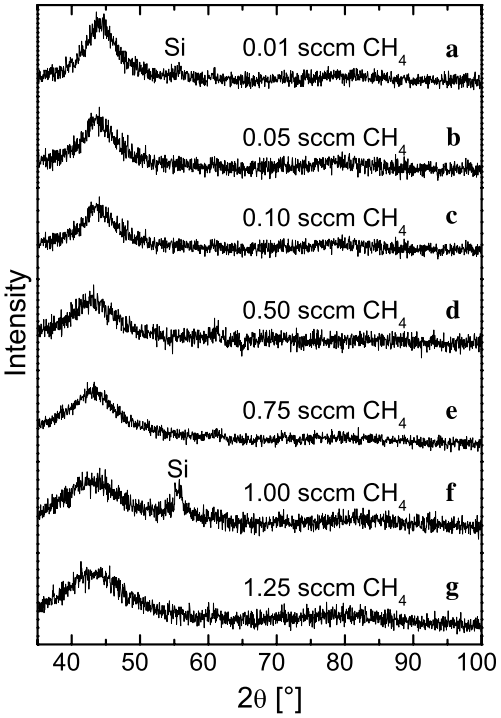

Fig. 4 GIXRD (2°) spectra of the carburized films. The CH_4 gas flows are given in the graph

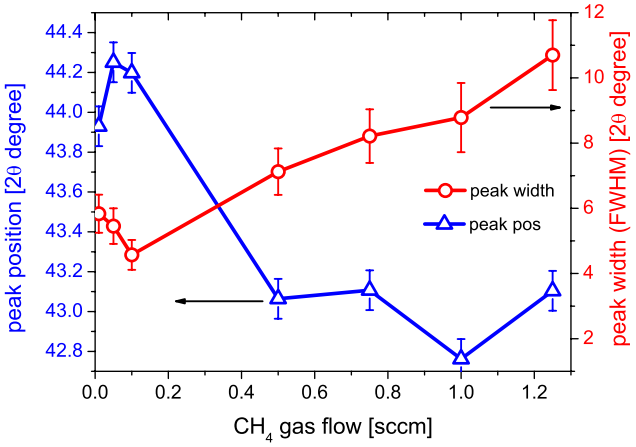

Fig. 5 Peak position and peak width of the first broad peak in the XRD spectra of the reactive sputtered stainless steel films

Figure 6 summarizes the CEMS measurements of the samples with increasing gas flow. They show the typical Mössbauer spectra of amorphous materials. Spectra in (a)–(c) are magnetically split, those in (e)–(g) are non-magnetic, where the spectrum in (d) shows both parts. This observation is consistent with the XRD results in Fig. 4. The results of the fitting procedures are presented in Table 2.

The spectra were fitted by hyperfine field distributions, and with quadrupole splitting distributions in the paramagnetic state, respectively. These distributions are attributed

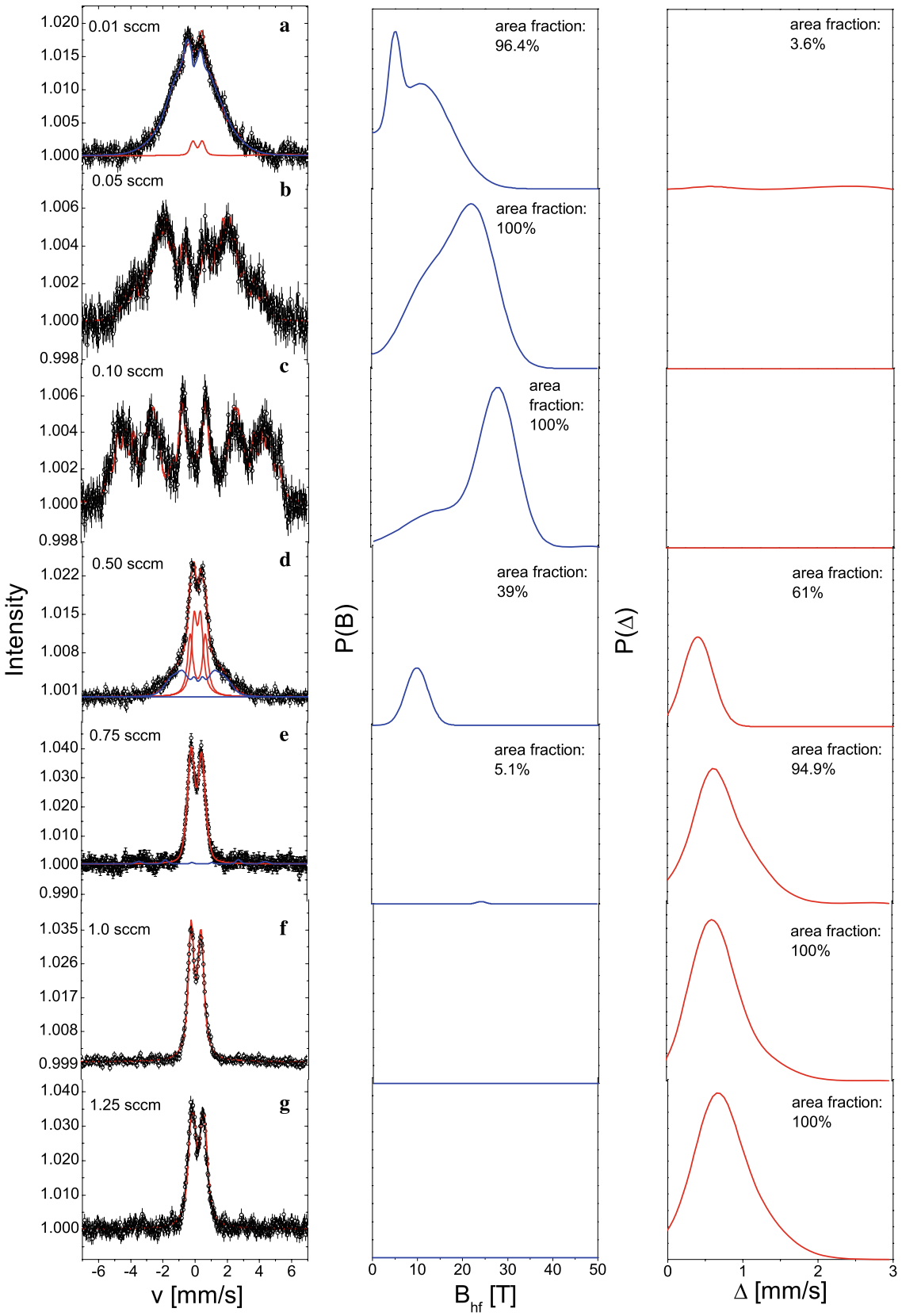

Fig. 6 Mössbauer spectra of the reactive sputtered AISI 316 films. The numbers in the graphs represent the methane gas flow

Table 2 Mössbauer fitting results of the carburized AISI 316 samples, deposited at room temperature with a magnetron power of 100 W (f—area fraction (error), mean values of $\langle\delta\rangle$—isomer shift, $\langle\Delta\rangle$—the quadrupole splitting for the paramagnetic subspectra, $\langle\epsilon\rangle$ the quadrupole splitting for the magnetic subspectra, B—hyperfine field)

CH_4 [sccm]	Part	f [%]	$\langle\delta\rangle$ [mm/s]	$\langle\Delta\rangle$, $\langle\epsilon\rangle$ [mm/s]	σ_Δ [mm/s]	$\langle B\rangle$ [T]	σ_B [T]
0.01	ferro-l	84.0(3)	−0.04	0.03		10.8(5)	6.7(4)
	ferro-h	12.4(5)	−0.04	0.03		4.9(4)	1.3(7)
	para	3.6(3)	0.15	0.58	0.24		
0.05	ferro-l	58.0(50)	−0.03	−0.05		23.2(24)	4.8(12)
	ferro-h	42.0(37)	−0.03	−0.05		12.7(55)	5.7(23)
0.10	ferro-l	68.2(9)	0.02	−0.02		27.8(5)	4.1(5)
	ferro-h	31.8(5)	0.02	−0.02		15.0(6)	7.9(35)
0.50	ferro	39.0(5)	0.19	0.00		9.7(4)	2.5(9)
	para-1	31.2(2)	0.14	0.40	0.20		
	para-2	29.8(1)	0.16	0.93	0.20		
0.75	ferro	5.1(3)	0.48	0.00		24.3(9)	1.0(2)
	para	94.9(8)	0.13	0.70	0.38		
1.00	para	100.0(1)	0.14	0.69	0.38		
1.25	para	100.0(1)	0.14	0.76	0.42		

to an amorphous stainless steel carbon-alloy, possibly rich in carbon. The quadrupole splittings are broad and close to the values of the usual carbides. Not much information can therefore be taken from them. Summarizing, all samples appear as an amorphous material which shows magnetic behavior below a gas flow of 0.75 sccm.

These Mössbauer results were confirmed by MOKE measurements. Figure 7 shows the result of the MOKE measurement of the 0.01 sccm CH_4 sample. The sample carburized with a gas flow of 0.05 sccm CH_4 shows an identical MOKE appearance.

A uniaxial anisotropy of about 70% can be seen with the maximum of the remanence around 150°. This behavior could be due to magnetostriction effects by stresses in the film. The coercive field H_C of both samples is approximately 4 Oe. Figure 7(b) shows the MOKE result of the as-carburized sample sputtered with 0.1 sccm CH_4 gas flow. It exhibits only a weak (fourfold) anisotropy, which is normally observed for an fcc phase [24, 31]. The coercive field was derived as 30 Oe. The samples with CEMS spectra shown in Fig. 6(d)–(g) do not show any magnetic behavior (e.g., no hysteresis loops in MOKE), which is in good agreement. These observations have now to be correlated to the carbon content of the film.

The EDX analyses of the deposited films revealed the original composition of the sputtering targets within the experimental limits. Unfortunately, the EDX did not allow to accurately determine elements lighter than oxygen. Therefore, in order to evaluate the amount of incorporated carbon, RBS measurements were carried out, whose results are shown in Fig. 8.

The thickness of the films as obtained from the RBS analysis was already given in Table 1. The carbon concentration of the films as obtained from the RBS analysis is given in Fig. 9 and can reach almost 70 at.%. There seems to be a clear correlation (parabolic-like) of the carbon content with the CH_4 gas flow, with a minimum close to 25% carbon for 0.5 sccm CH_4 flow. Unfortunately, RBS cannot distinguish between free carbon and carbon dissolved in the film.

The C-content as achieved by the RBS analyses exceeds the limit of 25 at.% for Fe_3C. Therefore, excessive carbon could eventually form graphite distributed in the film or on the surface of the film, but no signs of graphite could be detected in XRD. On the other hand, amorphous carbon would be difficult to see. To clarify this, we performed an AFM measurement which is shown in Fig. 10 for the sample sputtered with a CH_4 gas flow of 0.01 sccm.

Nanoscaled surface structures with the shape of half eggs can be observed. This shape is typical for carbon nanoclusters [32]. The clusters have a size between 10 and 80 nm in diameter and the roughness of the film is $R_a = 3$ nm. This method is not able to show the type of chemical bonding of the carbon clusters. Thus, we examined the carburized samples by means of Raman spectroscopy, which is displayed in Fig. 11.

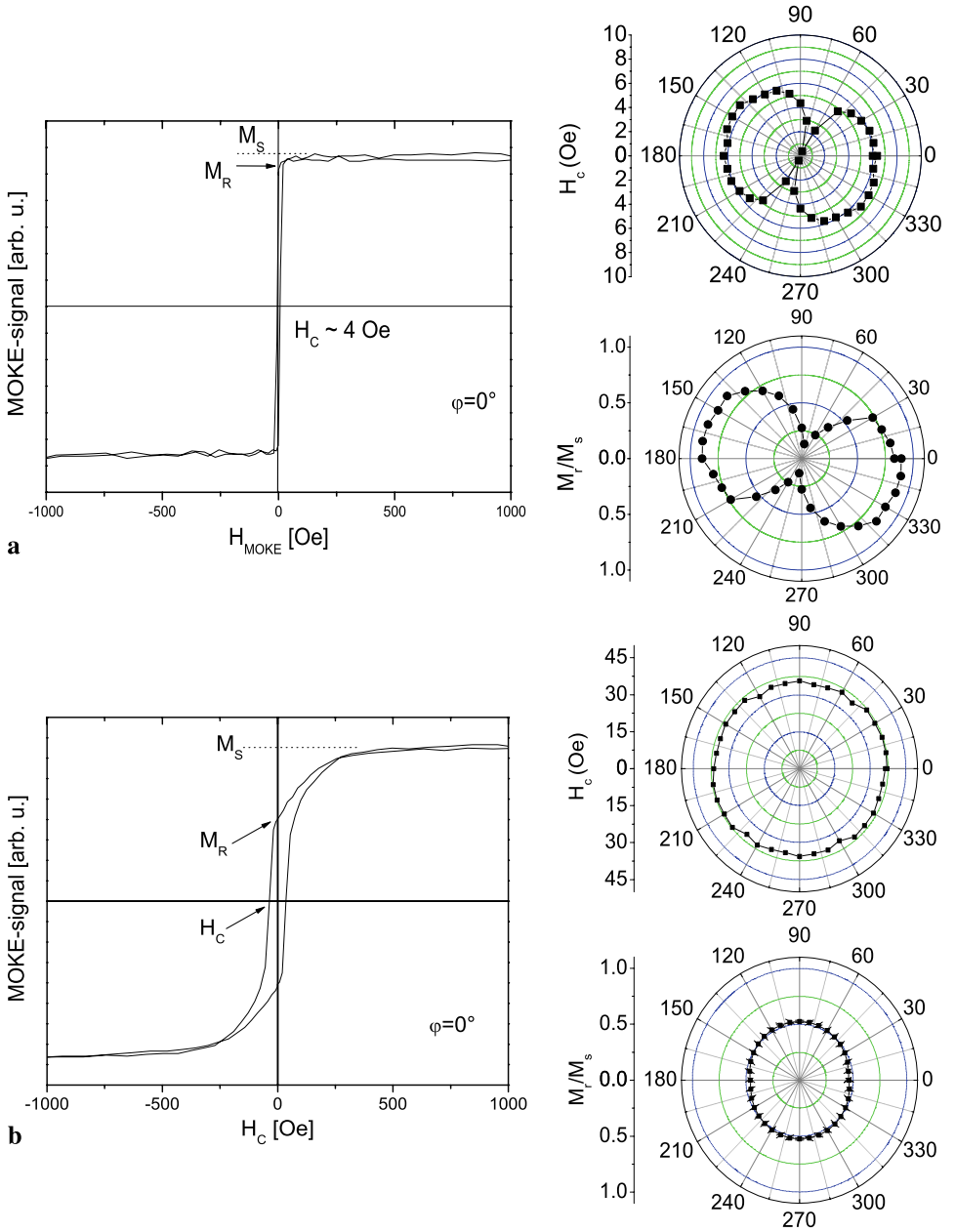

Fig. 7 Hysteresis curves of the reactive sputtered films with: (**a**) (*top*) 0.01 sccm CH_4 and (**b**) (*bottom*) 0.10 sccm CH_4 gas flow. The hysteresis is shown for sample at $\varphi = 0°$ (*left*) and polar diagrams of the coercive field H_C and the relative remanence M_R/M_S (*right*)

The Raman results show a narrow weak peak at a Raman shift of 1550 cm^{-1} for the soft ferromagnetic phase found in carburized thin AISI 316 (at 0.01 sccm CH_4 gas flow) and AISI 310 (at 0.05 sccm CH_4 gas flow) films. In literature [33], this shift has been attributed to the carbon g-band (sp^2 hybridized C). No d-band is observed around 1300–1350 cm^{-1}. The low intensity and the narrow peak form is typical for nanoparticles. This is a hint that at least some carbon forms graphite nanoparticles at the surface. We can compare the overall carbon ratios of the different films. These are in good agreement with our RBS results. According to the method described in [34], we were able to determine the stress in the film on the basis of the Raman peak positions, which add up to 2.5–3.3 GPa. Note, no clear dependencies can be seen between the stress in the film and composition of the target material.

3.2 Vacuum annealing of films carburized at room temperature

In order to analyze the thermal stability of the amorphous soft ferromagnetic phase, we performed annealing at a temperature of 973 K. The exposition times were set to 1, 10, and 120 h. The Mössbauer results of this isothermal series are shown in Fig. 12.

The Mössbauer spectra show various subspectra which can be attributed to carbides. The observed carbides and

their fractions support the carbide formation upon annealing and hint to the carbide transformation $M_3C/M_7C_3 \rightarrow M_{23}C_6 \rightarrow M_6C$ with increasing exposition time [5]. The Mössbauer results are summarized in Table 3.

The hyperfine parameters after annealing for 1 h are well-defined and the quadrupole doublets can be identified as M_3C/M_7C_3 carbides [7, 8]. The observed α-Fe sextet can be interpreted as bcc Fe probably containing some Ni, but almost no Cr and Mo [35]. After 10 h annealing, the doublets were identified as $M_{23}C_6$ according to [8, 36] and an α-Fe sextet as before. After 120 h vacuum annealing, the doublets can be identified as M_6C [6]. The corresponding XRD patterns are shown in Fig. 13.

The XRD pattern are in good agreement with the Mössbauer results. The mixed carbides $M_7C_3/M_{23}C_6/M_6C$ are observed. In consideration of these data, the transformations during annealing can be understood as follows [7, 8, 10, 37]: carbon diffuses out of the amorphous matrix and forms Cr-rich carbides, which further enriches in Cr and further transforms with increasing exposition time. The remaining matrix is more and more enriched in Ni and then transforms to γ. The α-Fe(110) peak and the M_7C_3-peak are overlapping, first this peak consists mostly of α-Fe which is then more and more transformed into M_7C_3. In the bottom-most XRD pattern it is only M_7C_3. Any supersaturated dissolved carbon tries to segregate and is used for carbide formation. A closer look to the stoichiometry shows an decrease of the C-content in the carbides with annealing time, from M_7C_3 over $M_{23}C_6$ to M_6C.

SEM pictures show that the excessive C diffuses also towards the surface and there forms nanowires, as seen in Fig. 14.

In addition, Raman spectroscopy was used to examine the bond behavior of the carbon after annealing. The spectra are shown in Fig. 15.

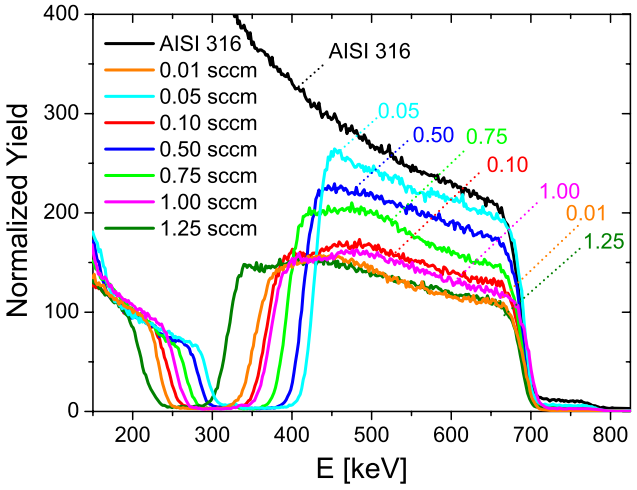

Fig. 8 RBS spectra of the reactively sputtered films. The CH_4 flow is given in the graph

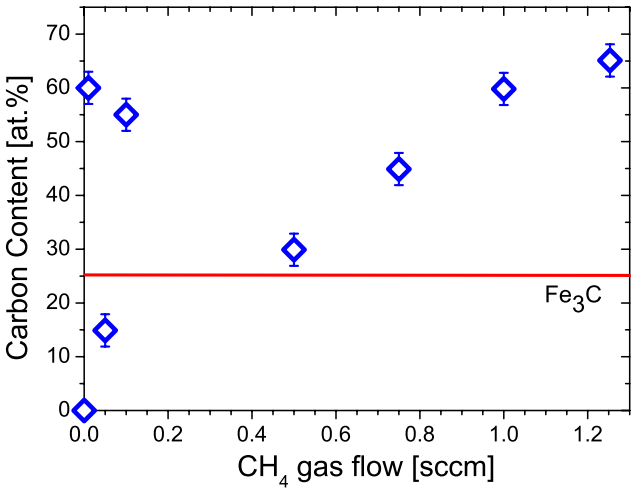

Fig. 9 Carbon content in the reactively sputtered films as derived from the RBS analysis versus the CH_4 gas flow

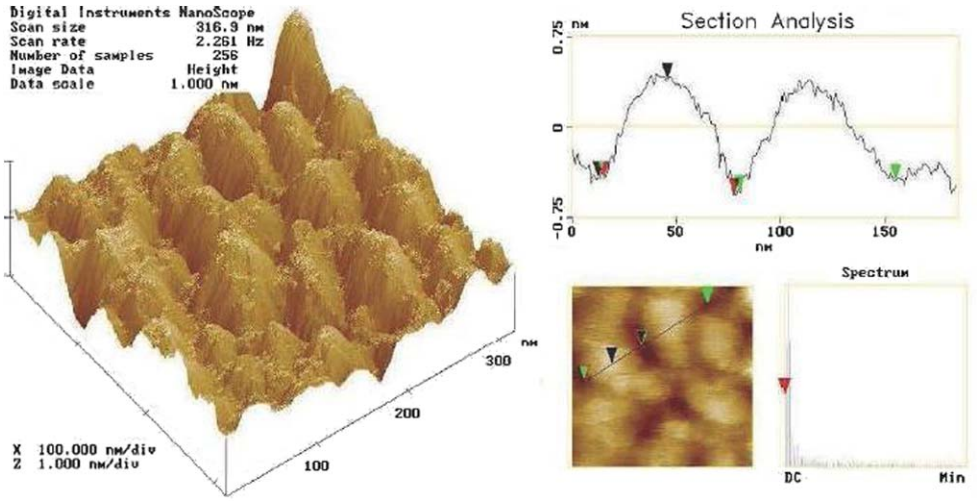

Fig. 10 AFM measurement (*left*) and cross section analysis (*right*) of the sample sputtered with a CH_4 gas flow of 0.01 sccm. The cross section analysis (*right bottom*) shows the line from which the roughness and the cluster-size were derived

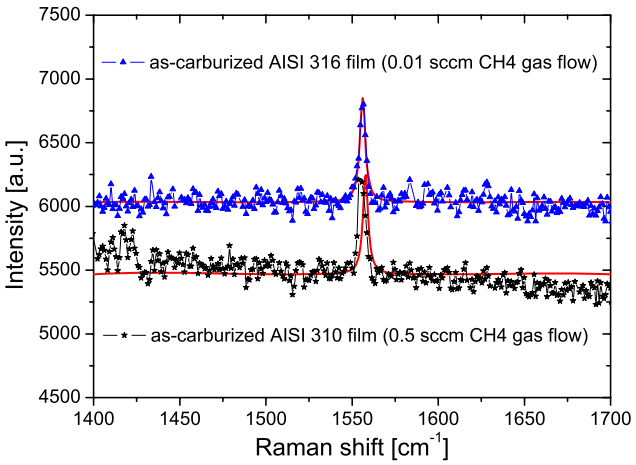

Fig. 11 Raman results for the amorphous soft ferromagnetic carburized AISI 310 and AISI 316 films

Both sp^2- and sp^3-hybridized carbon is observed. According to the three stage model of Ferrari et al. [38]

$$I_D/I_G = C'(\lambda) \cdot L^2{}_a, \quad (1)$$

where I_D and I_G are the intensities of the D and G peak, C the Raman coupling coefficient (C' (514.5 nm) = 0.0055), and L_a the cluster size, we were able to derive the sp^2/sp^3 ratio and thus the cluster size, which is in good agreement to AFM measurements. The results are given in Table 4.

Finally we were also able to embed our samples in the ternary phase diagram of amorphous carbon, which can be attributed to sputtered a-C. The weak and narrow peak at 1550 cm^{-1} again implies nanoclustering of graphite on the surface of the samples.

3.3 The influence of deposition temperature

In Fig. 16 the CEM spectra of carburized AISI 316 films deposited at increasing substrate temperatures are shown.

The deposition temperature clearly changes the nature of the deposited films, as seen by the changes in the spectra. It seems that at higher temperatures, the low B region has transformed in a non-magnetic quadrupole distribution. RBS show a decrease of carbon content from 60(2) % to 30(2) %, which affects the XRD pattern, in which a more clearer formation of the γ-phase is observed. The decrease of the carbon content originates in the formation of carbon-oxides or -hydroxides, which shade again into the vapor phase. The Mössbauer results are given in Table 5.

Consequently, the long-range diffusion process and thus the suppression of nucleation are less severe at higher deposition temperatures.

In Fig. 17 the XRD diffraction patterns are shown, the bars indicate the Bragg positions of the different reflexes as indicated.

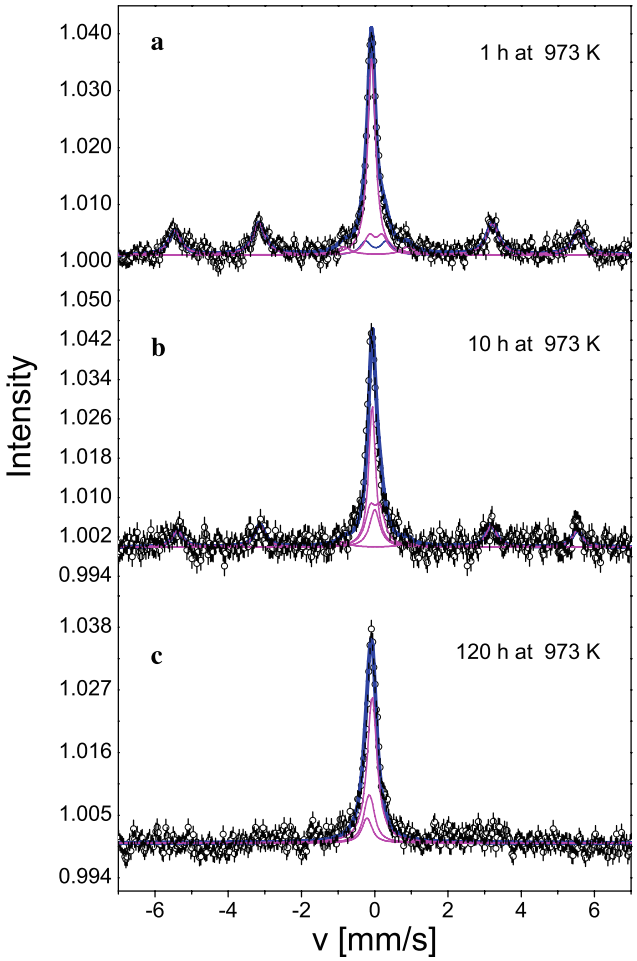

Fig. 12 Mössbauer spectra of vacuum annealed AISI 316 film sputtered with a magnetron power of 100 W and 0.01 sccm methane. Exposition time and temperature are given

At 298 K the amorphous phase dominates. At 673 K, a partial recrystallization process can be observed by the formation of carbides, but the amorphous character of the sample is maintained. Discrepancies in the peak positions imply the presence of stress in the films.

The results for the deposition temperature of 473 K were not reproducible, especially the Mössbauer spectra showed different grades of oxidation. We think, this is due to an enhanced plasma interaction between CH_4-radicals and oxygen. As a consequence of this, these results were not shown.

Figure 18 shows the MOKE measurement of the sample sputtered at 673 K. A weak fourfold anisotropy can be observed, which is typical for fcc phases [39]. The coercive field is about 6 Oe. This is in good agreement with the CEMS and GIXRD results. Deposition temperature is not as critical in phase formation as shown in inert sputtered AISI 316 stainless-steel films. The amorphous soft ferromagnetic phase mostly remains.

Table 3 Mössbauer results for the vacuum annealed sample deposited with 0.01 sccm methane flow (δ—isomer shift, Δ—the quadrupole splitting for the paramagnetic subspectra, ϵ the quadrupole splitting for the magnetic subspectra, B—hyperfine field, Γ—line width (HWHM), f—area fraction)

Annealing time [h]	Subspectrum	δ [mm/s]	Δ, ϵ [mm/s]	B [T]	Γ [mm/s]	f [%]
1	γ	−0.08(2)			0.12(8)	35.2(1)
	M_3C/M_7C_3	0.03(5)	0.35(4)		0.18(2)	12.0(4)
	M_3C/M_7C_3	0.04(5)	0.57(4)		0.17(8)	12.2(5)
	α-Fe (Ni)	0.04(5)	0.09(5)	34.2(2)	0.20(3)	40.6(6)
10	γ	−0.074(5)			0.13(10)	28.7(4)
	$M_{23}C_6$	0.00(5)	0.17(8)		0.18(12)	16.6(5)
	$M_{23}C_6$	0.01(1)	0.26(2)		0.18(8)	22.2(3)
	α-Fe (Ni)	0.04(2)	0.02(4)	33.8(4)	0.17(6)	32.5(8)
120	γ	−0.07(11)			0.16(1)	66.3(4)
	M_6C	−0.21(11)	0.08(4)		0.15(7)	11.3(2)
	M_6C	−0.15(7)	0.10(5)		0.15(11)	22.4(4)

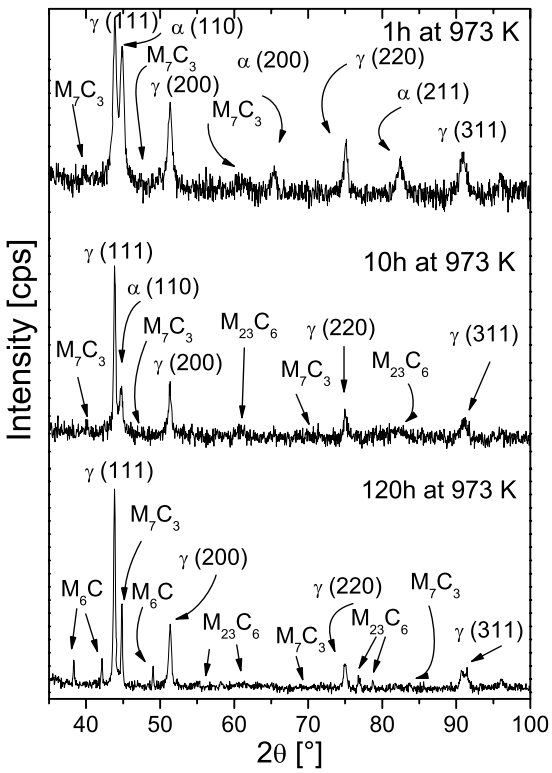

Fig. 13 GIXRD (2° incidence angle) spectra of the post-vacuum annealed samples sputtered with a magnetron power of 100 W and 0.01 sccm methane. Annealing temperature and time are given

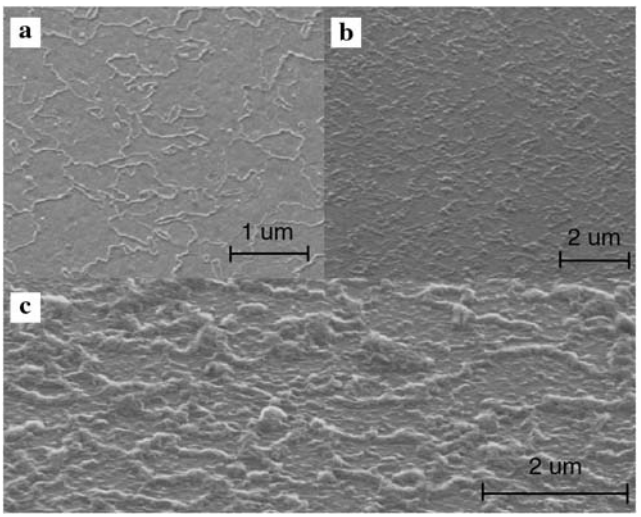

Fig. 14 SEM pictures of the post-vacuum annealed samples: (**a**) 1 h at 973 K, (**b**) 10 h at 973 K, and (**c**) 120 h at 973 K

4 Corrosion tests of carburized stainless steel films

In order to investigate the influence of the carburization on corrosion resistance, we performed corrosion tests on carburized stainless steel films, whose results are presented in Fig. 19.

A comparison of the two graphs provides the following differences between AISI 310 and AISI 316: the first peak at −1.3 V can be attributed to surface-diffused Cr. Note, the intensities in both steels are different due to the frequency of occurrence of the alloying elements. AISI 316 shows a better corrosion resistance in the passive area. In the range of −1 to −0.25 V it achieves negative current densities. Negative current densities are useful for the formation of oxides at the surface which increases the corrosion resistance. AISI 310 holds more Cr than AISI 316, but its current density rises again at −0.6 V. This can be attributed to the Ni surface-diffusion. The Richardson–Ellingham dia-

gram clearly shows that Ni has a bad oxide formation ability which could result in a worse corrosion resistance. Indeed, a certain Ni–Cr ratio is needed for an ideal corrosion resistance. This is given for AISI 316 [40]. The rising current density before the transpassive area is attributed to Mn surface-diffusion for AISI 310, and Mo surface-diffusion for AISI 316. The breakout potential for sputtered films is dominated by the Fe potential. The carburized AISI 316 sample sputtered at 298 K cannot be shown due to metallic disbandment, but its characteristics should be similar to those of the sample carburized at 673 K.

As a general observation, the corrosion resistance improves after carburization. More and more Cr (as well as Ni) diffuses to the surface and is used to form a thin oxide layer. This effect is less severe in the case of carburized AISI 316 films. The dimension of the corrosion resistance is given by the metallic disbandment. For inert sputtered AISI 316, we obtained a metallic disbandment at 3.5 V; 7 V for inert sputtered AISI 316 films sputtered at 673 K and 8 V for as-carburized AISI 316 films. Thus, carburization improves corrosion resistance by a factor of 2 in the case of AISI 316 films. As-sputtered AISI 310 films already have a high metallic disbandment (∼8 V). This can be attributed to the high Cr- and Ni-content. For similar carburizing conditions we obtained a metallic disbandment at 11 V for carburized AISI 310 films. This is an improvement by a factor of nearly 1.5, which is attributed to the disadvantageous Cr–Ni ratio in AISI 310. The substrate temperature during carburizing has a bigger influence on the corrosion resistance, but it has a marginal influence on the metallic disbandment. Finally, carburizing significantly improves the corrosion resistance.

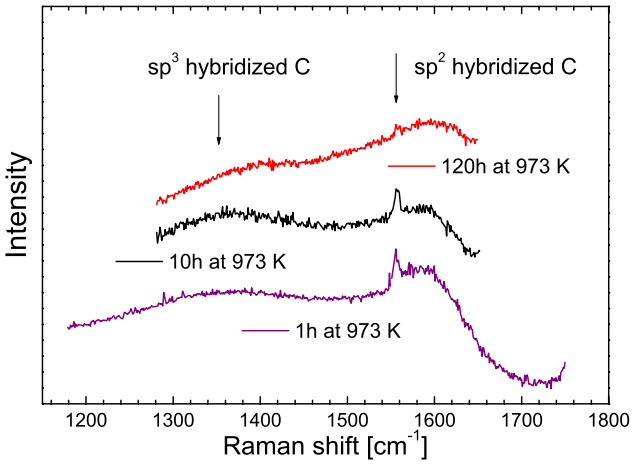

Fig. 15 Raman measurements of the post-vacuum annealed samples

5 Microhardness of carburized stainless steel films

Nanoindentation was performed to achieve an understanding of the influence of carburization on the microhardness

Table 4 Raman results of the vacuum-annealed samples

Annealing time at 973 K [h]	I_D/I_G	L_a [nm]
1	0.53(3)	10(1)
10	0.85(2)	12(2)
120	0.75(1)	12(1)

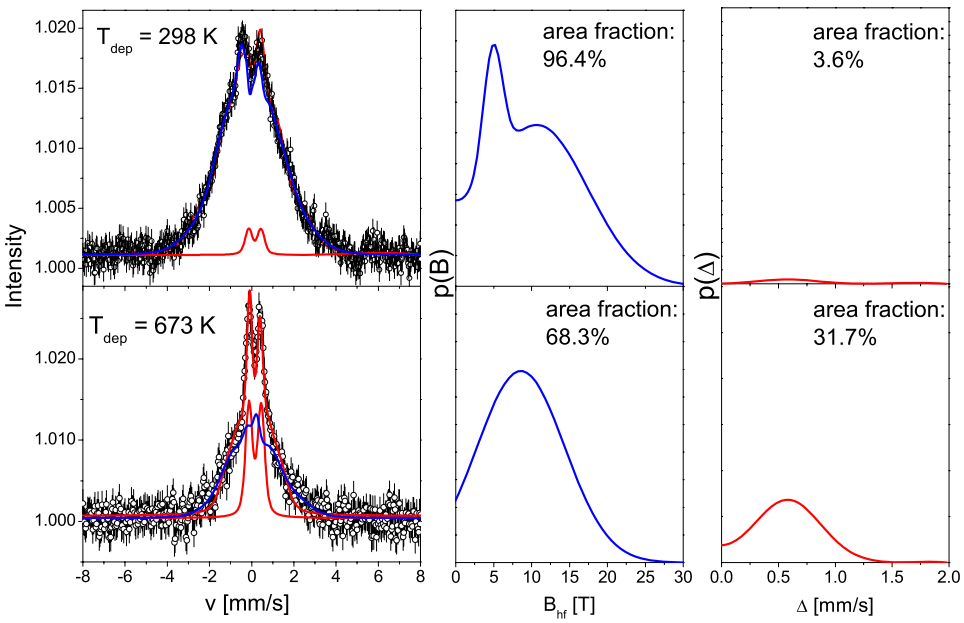

Fig. 16 CEM spectra of carburized AISI 316 films sputtered with a magnetron power of 100 W and 0.01 sccm methane at two temperatures: T = 298 K (*top*), T = 673 K (*bottom*). On the right hand side, the hyperfine field distribution $p(B)$ and the quadrupole splitting distribution $p(\Delta)$ are shown

Table 5 CEM results of AISI 316 films, deposited at 673 K with a magnetron power of 100 W and 0.01 sccm CH_4 flow (f—area fraction (error), mean values of δ—isomer shift, $\langle\Delta\rangle$—the quadrupole splitting for the paramagnetic subspectra, $\langle\epsilon\rangle$ the quadrupole splitting for the magnetic subspectra, B—hyperfine field)

CH_4 [sccm]	Part	f [%]	$\langle\delta\rangle$ [mm/s]	$\langle\Delta\rangle, \langle\epsilon\rangle$ [mm/s]	σ_Δ [mm/s]	$\langle B\rangle$ [T]	σ_B [T]
0.01	ferro	68.3(4)	0.17	0.12		8.6(2)	5.7(2)
	para-1	29.2(2)	0.16	0.59	0.28		
	para-2	0.4(2)	−0.10	0.10	0.04		
	para-3	2.1(3)	0.17	0.50	0.04		

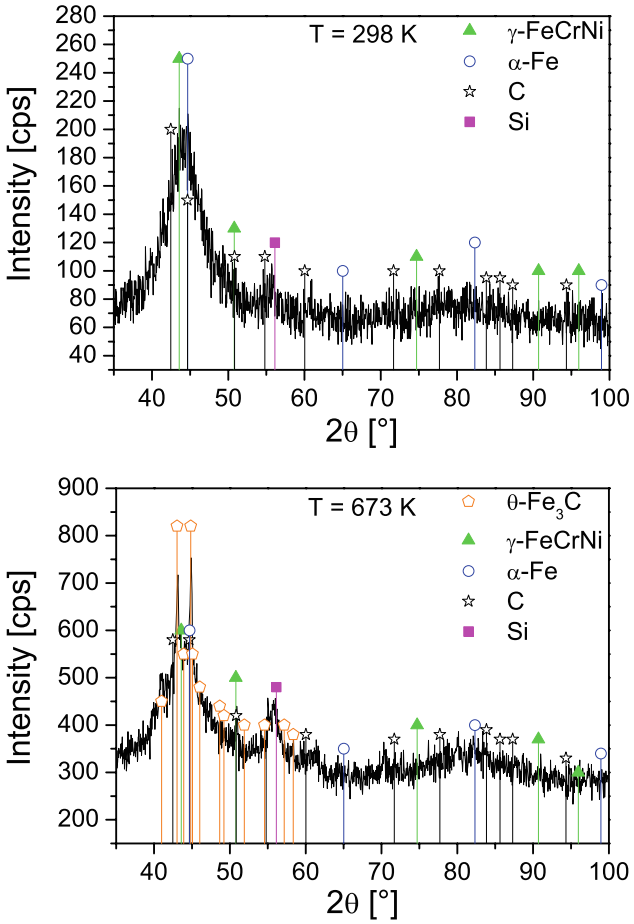

Fig. 17 GIXRD (2° incidence angle) spectra of the as-carburized samples sputtered with a magnetron power of 100 W and 0.01 sccm methane. The substrate temperatures are given

and the mechanical properties. The results are presented in Tables 6 and 7, where also the carbon content derived from RBS is included.

Different dependencies were observed for the different steel types. While the C-content rises quite linearly in carburized AISI 310 films with the methane gas flow, no clear dependencies are obtained for AISI 316 films. Both phenomena can be explained with the model of Lux and Haubner [41] mentioned in the discussion area. In the case of carburized AISI 310 films, all carbon is used to form carbides and graphite from the vapor phase. For carburized AISI 316 films we assume a higher and faster plasma interaction between CH_x radicals and sputter-adsorbates which can deplete already existing carbides or graphite. The hardness values for the amorphous soft ferromagnetic phases are conspicuous. For AISI 310, this phase exhibits the lowest hardness. Amorphous carburized AISI 316 is the hardest sample. Given that the microstructure of these amorphous soft ferromagnetic phases is unknown, no explanation is obvious for that. Further EXAFS and DSC experiments might help to understand the nature of this phase.

Table 6 Hardness, Young modulus and C-content of carburized AISI 310 films, where E is the elastic modulus an v the Poisson ratio

CH_4 Gas flow [sccm]	Hardness [GPa]	Young modulus $E/(1-v^2)$ [GPa]	C-content [at. %]
0.10	6.1(5)	129(2)	39.75
0.50	3.4(2)	98(1)	29.90
0.75	4.3(3)	101(1)	52.10
1.00	7.3(2)	166(3)	52.90
1.25	5.8(3)	120(2)	65.80

Table 7 Hardness, Young modulus, and C-content of carburized AISI 316 films, where E is the elastic modulus an v the Poisson ratio

CH_4 Gas flow [sccm]	Hardness [GPa]	Young modulus $E/(1-v^2)$ [GPa]	C-content [at. %]
0.01	5.2(4)	113(1)	60.0
0.05	4.8(1)	105(1)	14.9
0.10	5.1(3)	108(1)	55.0
0.50	4.1(5)	98(1)	29.9
0.75	5.1(2)	108(1)	44.9
1.00	4.4(9)	97(1)	59,8
1.25	4.0(1)	88(1)	65.1

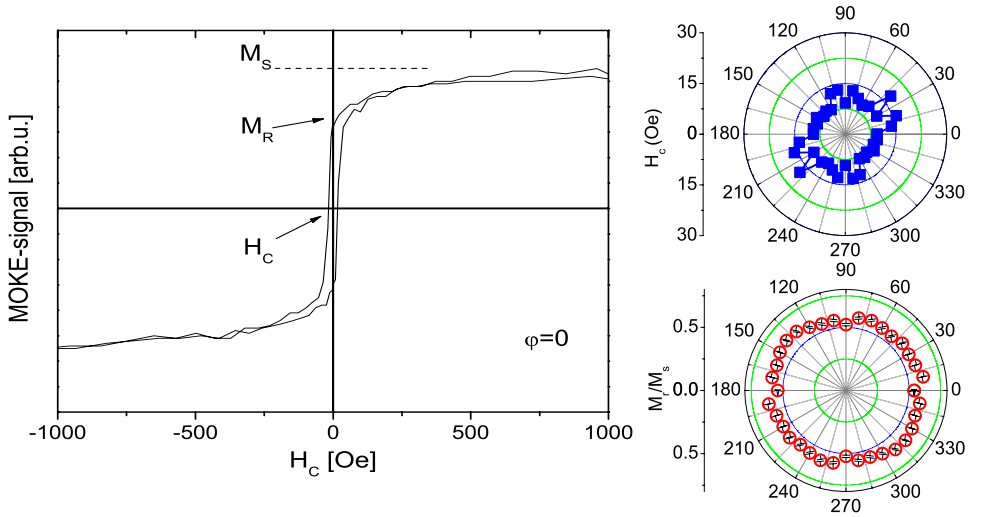

Fig. 18 Hysteresis curve of the film sputtered at 673 K with 0.1 sccm CH_4 gas flow at $\varphi = 0°$ (*left*) and polar diagrams of the coercive field H_C and the relative remanence M_R/M_S (*right*)

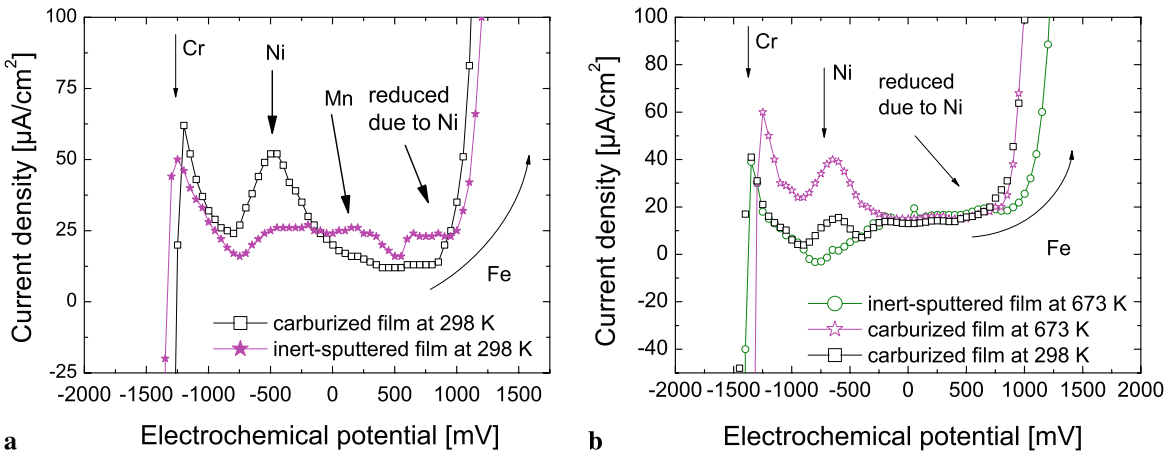

Fig. 19 Corrosion tests of AISI 310 (**a**) and AISI 316 (**b**) sputtered films. All samples were sputtered at a magnetron power of 100 W, inert-sputtered sample with 12 sccm Ar gas flow, carburized samples with 0.01 sccm CH_4 gas flow. Temperatures are given in the graphs

Table 8 Carbide Formation Ability (CFA) of AISI steels. The lattice constants a are also given

Element	Electron configuration	Atom radius [Å]	Crystallographic structure	a [Å]	CFA
Fe	$3d^6 4s^2$	1.260	BCC(α)	2.861	0.210
			FCC(γ)	3.564	
Cr	$3d^5 4s^2$	1.270	BCC	2.885	0.256
Ni	$3d^8 s^2$	1.250	FCC	3.520	0.156
Mn	$3d^5 4s^2$	1.270	SC(α)	8.894	0.254
			SC(γ)	6.300	
			FCC(γ)	3.774	
			BCC(δ)	3.720	
Mo	$4d^5 4s^1$	1.390	BCC	2.885	0.278

6 Discussion

Now three questions arise: how can the formation of the amorphous soft ferromagnetic phase be explained and how much carbon is incorporated in the films, which finally leads to the question of the carbide formation. According to Lu et al. [13] the first question can be answered as follows: the present Fe-based alloy is associated with the deep eutectic point of the Fe–C system. It is well known that compositions around the deep eutectic point are ideal for glass formation in many systems. As a result, glass formation is greatly favored thermodynamically. Further, the minor addition of Mo could promote glass formation in the Fe–C system by suppressing the formation of the primary phase (i.e., Fe carbides). Because of their limited solubility in Fe carbides, the molybdenum atoms must redistribute and long-range diffusion is required upon solidification. Thus, the minor addition of Mo could retard the nucleation process.

Another approach is the so-called Carbide Formation Ability (CFA) [42], which evaluates the effect of the composition elements. CFA is based on physicochemical analysis [42] of the carbide formation processes accompanying the primary and secondary crystallization of a weld metal with reliance on quantum-chemical theories that depict the structure of transition metals and carbides. CFA is defined as

$$\Theta_i = \frac{R_i}{d_i}, \tag{2}$$

where R_i is the radius of the alloy elements and d_i the number of the electrons in d-orbital. The CFAs of common steel elements are given in Table 8.

We assume that the growth mechanism of our fabricated stainless steel films is a combination of the pre-mentioned models. Whereas the first model prescribes that molybdenum aids a diffusion process which suppresses carbide formation, the CFA model predicts the highest CFA value for molybdenum. The fact that the present carburized steel system consists of five elements, the probability of each atom to interact only with one sort of element is not given. Thus, the CFA model can only be used auxiliary. A clear evidence of this hypothesis will be topic of further investigations, wherein the ion-distribution functions of carburization processes will be investigated.

In contrast to inert gas sputtered AISI 316 films, the role of Ni is insignificant. Even the method of instantaneous recording of the electromotive force (MIE) [28, 43] was inconclusive. The chemical potential of the films changed from Fe-potential at room temperature to Fe_2O_3-potential at 673 K. Thus, the Gibbs–Thomson effect cannot be used to explain the formation of carbides. This backs the thesis of long-range diffusion during nucleation. It can be assumed that—due to the relative abundances of the steel elements—these carbides are $(Fe, Cr)_3C$ carbides.

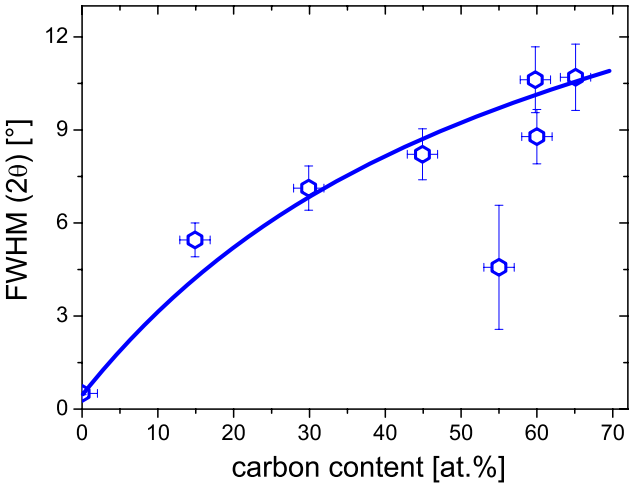

Fig. 20 Peak width of the first amorphous peak in dependence of the carbon content of reactive sputtered stainless steel films

In consideration to the present results we have an entire conception of the nucleation process which is referred by Lux and Haubner [41]. During the nucleation process carbonaceous species were adsorbed on the surface. Via vapor phase interaction, e.g., hydrogen recombination and formation of CH_x radicals, free C atoms were formed. Diffusion processes already inserted by Mo atoms solve the C atoms in the metal matrix. The carburization initially takes up all available C out of the vapor phase, until a closed carbide film is formed. With increasing thickness of the carbide film, the C transport in the metal matrix is slowed down. This leads to an increasing C-content on the surface which induces metastable clustering. The differing carbon content in the carburized stainless steel films is originated in the inserted diffusion process (and thus in the differing carbon take up in the metal matrix) which depends on the processing parameters. If the grain sizes exceeds a critical value, even diamond-like carbon films can be built [41].

This model explains the variety of the observed phases and the different carbon contents in the carburized films. It is reasonable to assume that the solubility limit of C in Fe_3C is reached. Excessive C-content exists in form of graphite nanoclusters on top of the film. This is confirmed by Fig. 20 which shows the dependence between peak width and carbon content.

A clear tendency can be seen: with higher carbon concentration, higher peak widths can be reached. Only the sample sputtered at 0.10 sccm CH_4 gas flow deviates. The first reflex in the XRD pattern of this sample had to be fitted with two peaks: one attributed to an amorphous phase and one attributed to a crystalline phase. It is reasonable to assume that all XRD pattern could be fitted by two peaks, but there are no clear hints (peak asymmetry, etc.) as seen for the 0.10 sccm sample. Even here, no quantitative conclusion can be given

how many carbon is solved in the metallic matrix as graphite or as carbide.

The structural nature of the amorphous soft ferromagnetic phase is still unknown, but we assume that Mo triggers a diffusion processes which suppresses the formation of carbides and should thus lead to a loss of distal-order and to a dramatic change in the liquidus temperature. With respect to this, differential scanning calorimetry (DSC) and extended X-ray absorption fine structure (EXAFS) analysis are in preparation to reach a full understanding of the microstructure of amorphous steels.

7 Conclusions

Various aspects of the carbide formation and the stability in magnetron carburized austenitic stainless-steel films were studied. The magnetic properties investigated by means of Mössbauer spectroscopy and MOKE showed the formation of various phases and carbides at a sputtering temperature of 298 K. In addition, a new amorphous soft ferromagnetic phase was observed and its thermal stability was studied. The microstructure could not be fully explained in this study, but we assume that Mo/Mn inserts a diffusion process which suppresses the formation of carbides and should thus lead to a loss of long-range order.

Vacuum annealing of the carburized amorphous soft ferromagnetic phase showed the carbide reaction $M_7C_3 \rightarrow M_{23}C_6 \rightarrow M_6C$. SEM pictures revealed that the excessive carbon diffuses to the surface and is used to form carbon nanowires. Raman spectroscopy revealed both the g-band and d-band of the carbon system. By means of the g-/d-band ratio, we could integrate our carburized samples in the ternary phase diagram of amorphous carbon.

Chemical stability was investigated by means of corrosion tests. Carburization improves the corrosion resistance by a factor of 1.5 for AISI 310, and by a factor of 2 for AISI 316. Carburized AISI 310 shows lower hardness than carburized AISI 316.

Acknowledgements We would like to thank Ingo Bergmann and Andreas Schenk from the Institute of Theoretical and Physical Chemistry, TU Braunschweig, for their help with the corrosion tests. Peter Schaaf gratefully acknowledges the kind support of the Deutsche Forschungsgemeinschaft (DFG grant Scha 632/11).

References

1. J. Kunze, *Nitrogen and Carbon in Iron and Steel* (Akademie Verlag, Berlin, 1990)
2. M. Hillert, C. Qiu, Metall. Trans. A **22**, 2187–2198 (1991)
3. P. Schaaf, Prog. Mater. Sci. **47**(1), 1–161 (2002)
4. H.-J. Grabke, E. Müller-Lorenz, A. Schneider, ISIJ Int. **41**(Suppl.), 1–8 (2001)
5. A. Inoue, T. Masumoto, Metall. Trans. A Phys. Metall. Mater. Sci. **11**(5), 739–747 (1980)
6. F. Gauzzi, C. Lupi, B. Verdini, G. Principi, Hyperfine Interact. **69**(1–4), 541–544 (1991)
7. P. Schaaf, S. Wiesen, U. Gonser, Acta Metall. Mater. **40**(2), 373–379 (1992)
8. P. Schaaf, A. Krämer, S. Wiesen, U. Gonser, Acta Metall. Mater. **42**(9), 3077–3081 (1994)
9. P. Schaaf, P. Bauer, U. Gonser, Z. Met. Kd. **80**(2), 77–82 (1989)
10. E. Carpene, P. Schaaf, Appl. Phys. Lett. **80**(5), 891–893 (2002)
11. S. Cusenza, M. Seibt, P. Schaaf, Appl. Surf. Sci. **254**(4), 955–960 (2007)
12. D.H. Xu, G. Duan, W.L. Johnson, Phys. Rev. Lett. **92**(24), 245504 (2004)
13. Z.P. Lu, C.T. Liu, J.R. Thompson, W.D. Porter, Phys. Rev. Lett. **92**(24), 245503 (2004)
14. V. Ponnambalam, S.J. Poon, G.J. Shiflet, V.M. Keppens, R. Taylor, G. Petculescu, Appl. Phys. Lett. **83**(6), 1131–1133 (2003)
15. P. Schaaf, A. Kramer, L. Blaes, G. Wagner, F. Aubertin, U. Gonser, Nucl. Instrum. Methods Phys. Res. Sect. B Beam Interact. Mater. Atoms **53**(2), 184–186 (1991)
16. P. Schaaf, L. Blaes, J. Welsch, H. Jacoby, F. Aubertin, U. Gonser, Hyperfine Interact. **58**(1–4), 2541–2545 (1990)
17. U. Gonser, P. Schaaf, F. Aubertin, Hyperfine Interact. **66**(1–4), 95–100 (1991)
18. P. Schaaf, A. Emmel, E. Schubert, H.W. Bergmann, K.P. Lieb, Hyperfine Interact. **92**(1–4), 1361–1366 (1994)
19. P. Schaaf, U. Gonser, Hyperfine Interact. **57**(1–4), 2101–2104 (1990)
20. P. Schaaf, Hyperfine Interact. **111**(1–4), 113–119 (1998)
21. R.A. Brand, NORMOS—Mössbauer fitting program (1999)
22. F. Landry, P. Schaaf (1996, unpublished)
23. G.A. Müller, R. Gupta, K.P. Lieb, P. Schaaf, Appl. Phys. Lett. **82**(1), 73–75 (2003)
24. G.A. Müller, E. Carpene, R. Gupta, P. Schaaf, K. Zhang, K.P. Lieb, Eur. Phys. J. B **48**(4), 449–462 (2005)
25. G.A. Müller, K.P. Lieb, E. Carpene, K. Zhang, P. Schaaf, J. Faupel, H.U. Krebs, Hyperfine Interact. **158**(1–4), 137–143 (2004)
26. M. Uhrmacher, K. Pampus, F.J. Bergmeister, D. Purschke, K.P. Lieb, Nucl. Instrum. Methods Phys. Res. Sect. B Beam Interact. Mater. Atoms **9**(2), 234–242 (1985)
27. P. Schaaf, C. Illgner, F. Landry, K.P. Lieb, Surf. Coat. Technol. **101**(1–3), 404–407 (1998)
28. S. Cusenza, C. Borchers, E. Carpene, P. Schaaf, J. Phys. Condens. Matter **19**(10), 106211 (2007)
29. P. Schaaf, V. Biehl, U. Gonser, M. Bamberger, P. Bauer, J. Mater. Sci. **26**(18), 5019–5024 (1991)
30. P. Schaaf, P. Bauer, U. Gonser, Hyperfine Interact. **46**(1–4), 541–548 (1989)
31. K. Zhang, R. Gupta, K.P. Lieb, Y. Luo, G.A. Müller, P. Schaaf, M. Uhrmacher, J. Magn. Magn. Mater. **272**(76), 1162–1163 (2004)
32. A. Göhl, B. Günther, T. Habermann, G. Müller, M. Schreck, K. Thurer, B. Stritzker, J. Vac. Sci. Technol. B **18**(2), 1031–1034 (2000)
33. F. Tuinstra, J.L. Koenig, J. Chem. Phys. **53**(3), 1126 (1970)
34. H. Harima, J. Phys. Condens. Matter **14**(38), R967–R993 (2002)
35. F.S. Li, J.J. Sun, C.L. Chien, J. Phys. Condens. Matter **7**(9), 1921–1931 (1995)
36. M. Vardavoulias, G. Papadimitriou, Phys. Status Solidi A Appl. Res. **134**(1), 183–191 (1992)

37. P. Schaaf, M. Kahle, E. Carpene, Appl. Surf. Sci. **247**(1–4), 607–615 (2005)
38. A.C. Ferrari, J. Robertson, Phys. Rev. B **61**(20), 14095–14107 (2000)
39. K. Zhang, R. Gupta, K.P. Lieb, Y. Luo, G.A. Müller, P. Schaaf, M. Uhrmacher, Europhys. Lett. **64**(5), 668–674 (2003)
40. H. Kaesche, *Corrosion of Metals, Physicochemical Principles and Current Problems* (Springer, Berlin, 2003)
41. B. Lux, R. Haubner, Nucleation and growth of low-pressure diamond, in *Diamond and Diamond-like Films and Coatings* (Plenum, New York, 1991)
42. V. Mazurovsky, M. Zinigrad, L. Leontiev, V. Lisin, Carbide formation during crystallization upon welding, in *Third International Conference on Mathematical Modeling and Computer Modeling and Computer Simulation of Materials Technologies MMT* (2004)
43. R.N. Rostovtsev, Met. Sci. Heat Treat. **44**, 211–213 (2002)